Lv, Zhong-Peng; Srivastava, Divya; Conley, Kevin; Ruoko, Tero-Petri; Xu, Hongyi; Lightowler, Molly; Hong, Xiaodan; Cui, Xiaoqi; Huang, Zhehao; Yang, Taimin; Wang, Hai-Ying; Karttunen, Antti J.; Bergström, Lennart

Visualizing Noncovalent Interactions and Property Prediction of Submicron-Sized Charge-Transfer Crystals from ab-initio Determined Structures

Published in:
Small Methods

DOI:
10.1002/smtd.202301229

Published: 19/07/2024

Document Version
Publisher's PDF, also known as Version of record

small methods
www.small-methods.com

Visualizing Noncovalent Interactions and Property Prediction of Submicron-Sized Charge-Transfer Crystals from *ab-initio* Determined Structures

Zhong-Peng Lv, Divya Srivastava, Kevin Conley, Tero-Petri Ruoko, Hongyi Xu, Molly Lightowler, Xiaodan Hong, Xiaoqi Cui, Zhehao Huang, Taimin Yang,* Hai-Ying Wang,* Antti J. Karttunen, and Lennart Bergström*

The charge-transfer (CT) interactions between organic compounds are reflected in the (opto)electronic properties. Determining and visualizing crystal structures of CT complexes are essential for the design of functional materials with desirable properties. Complexes of pyranine (PYR), methyl viologen (MV), and their derivatives are the most studied water-based CT complexes. Nevertheless, very few crystal structures of CT complexes have been reported so far. In this study, the structures of two PYRs-MVs CT crystals and a map of the noncovalent interactions using 3D electron diffraction (3DED) are reported. Physical properties, e.g., band structure, conductivity, and electronic spectra of the CT complexes and their crystals are investigated and compared with a range of methods, including solid and liquid state spectroscopies and highly accurate quantum chemical calculations based on density functional theory (DFT). The combination of 3DED, spectroscopy, and DFT calculation can provide important insight into the structure-property relationship of crystalline CT materials, especially for submicrometer-sized crystals.

1. Introduction

In the past few decades, interactions between the electron-rich (donors, D) and electron-deficient (acceptors, A) molecules have gained considerable attention in organic electronics. This focus on D–A association has led to the exploration of charge-transfer complexes (CTCs).[1,2] The charge-transfer (CT) states at the D–A interface exhibit unique electronic and optoelectronic properties that hold great promise for organic electronics, such as organic field-effect transistors,[3,4] ferroelectrics,[5] organic photovoltaic cells,[6] and organic light-emitting devices.[7–9] To enable the rational design and controlled synthesis of CTCs, substantial efforts have been directed toward understanding the nature of CT states,[10–12] which is heavily influenced by the molecular structures and the noncovalent interactions between D and A molecules.[13] Thus, obtaining the crystal structure of the CTCs became significant for their application. Most well-studied CTC crystals are assembled in low-polarity organic solvents.[14,15] For water-soluble CTCs, though many low-dimension nano assemblies have been reported,[16] well-defined crystals are still sparse, because the complex noncovalent interactions in water always result in

Z.-P. Lv, X. Hong
Department of Applied Physics
Aalto University
Espoo FI 02150, Finland
E-mail: zhongpeng.lyu@aalto.fi
D. Srivastava, K. Conley, A. J. Karttunen
Department of Chemistry and Materials Science
Aalto University
Espoo FI 02150, Finland
T.-P. Ruoko
Faculty of Engineering and Natural Sciences
Tampere University
Tampere FI-33720, Finland
H. Xu, M. Lightowler, Z. Huang, T. Yang, L. Bergström
Department of Materials and Environmental Chemistry
Stockholm University
Stockholm SE 10691, Sweden
E-mail: taimin.yang@mmk.su.se
X. Cui
Department of Electronics and Nanoengineering
Aalto University
Espoo FI 02150, Finland
H.-Y. Wang
School of Environmental Science
Nanjing Xiaozhuang University
Nanjing 211171, P. R. China
E-mail: wanghaiying@nju.edu.cn

The ORCID identification number(s) for the author(s) of this article can be found under https://doi.org/10.1002/smtd.202301229

DOI: 10.1002/smtd.202301229

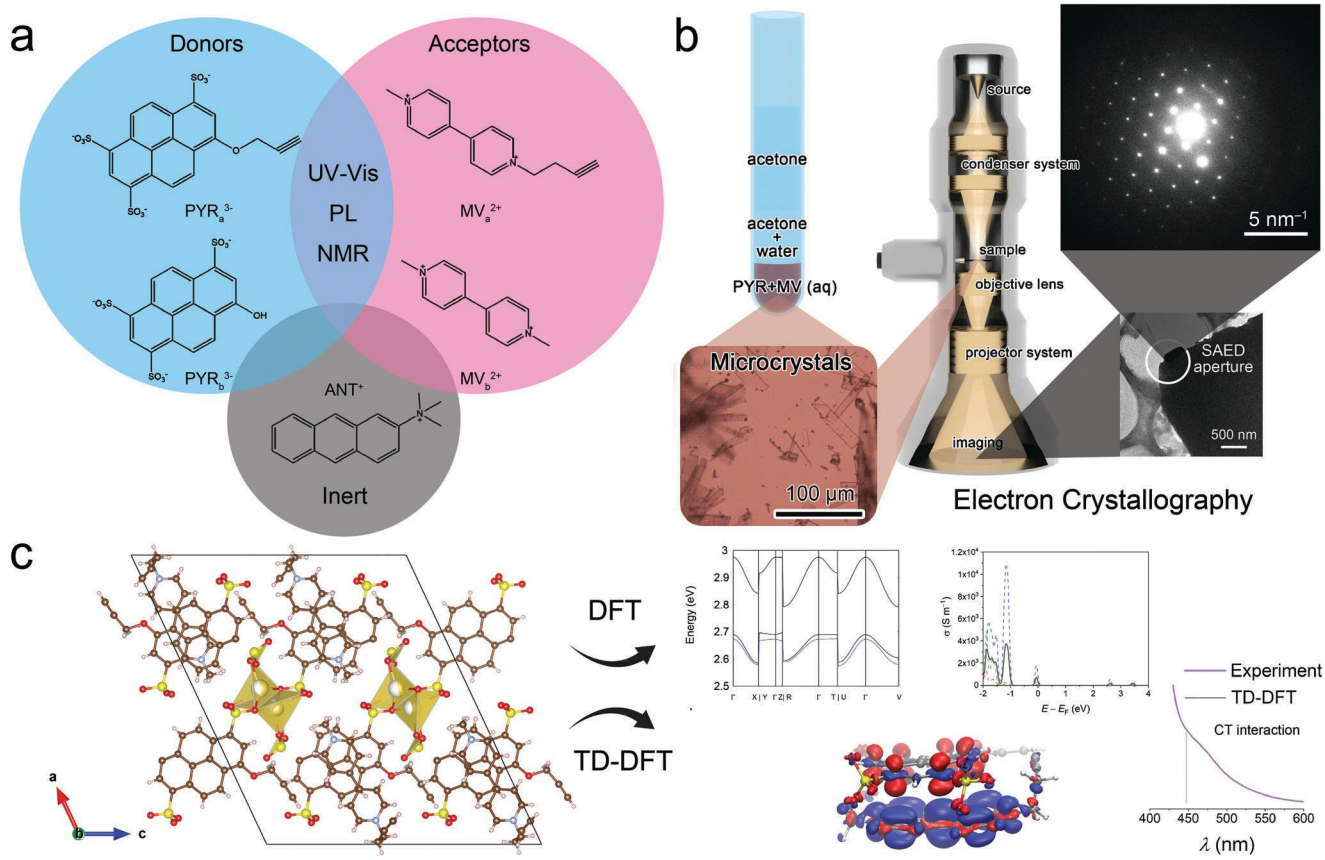

Scheme 1. A schematic illustration of the CTCs and major methodologies in the study. a) Chemical structures of the PYRs (D) and MVs (A) derivatives, as well as the inert ANT. Different methods such as UV–vis, PL, and NMR are used for characterizing the CT interactions. b) Schematic illustration of the three-layer diffusion method for the growth of PYR-MV microcrystals (left), and one of the selected area electron diffraction (SAED) patterns for crystal structural resolving (right). c) Resolved crystal structure of **PYR$_a$-MV$_a$** complex (left) and calculated band structure, the conductivity of the CTC solid, and electronic excitation in the aqueous phase compared with the experimental UV–vis spectrum (right).

submicron crystals which are too small for X-ray crystallography.[17] Consequently, there are very few reported water-soluble CTC crystal structures,[18,19] and their structure-property relationship is not well investigated.

Due to the stronger scattering ability of electrons than X-ray photons, 3D electron diffraction (3DED) can determine structures from submicron or nano-sized crystals, such as zeolites,[20,21] metal-organic frameworks (MOFs),[22,23] small organic molecules,[24] and proteins.[25] The high-resolution 3DED datasets can provide essential information on structural details, such as hydrogen atoms positions,[26] charge,[27] and molecular chirality.[28]

In this study, we use 3DED to obtain the high-accuracy structures of two submicron-sized CTCs crystals of pyranine (PYRs) and methyl viologen (MVs) derivatives (**Scheme 1a,b**). To the best of our knowledge, this is the first time that the crystal structures of aqueous CTCs were determined by 3DED. With the high-precision structures, we employed computational methods, e.g., density functional theory (DFT) and time-dependent DFT (TD-DFT),[29–32] to predict a range of physical properties such as electronic band structures, conductivities, CT mechanism, and optical excitations (Scheme 1c). In addition, we visualized different types of noncovalent interactions, including hydrogen bonding, electrostatic interaction, $\pi...\pi$ interactions, van der Waals (VDW) interactions, and CT interactions. The CT interactions and the packing geometries of the CTCs were also investigated using Ultraviolet-visible (UV–vis) spectroscopy, photoluminescence (PL) spectroscopy, and nuclear magnetic resonance (NMR). Additionally, we studied the interaction between the PYRs/MVs with another widely used CT molecule as a control (2-anthryltrimethylammonium, ANT).[33] With our combined experimental and theoretical investigation workflow, we have successfully visualized and comprehensively analyzed the CTCs of PYRs and MVs in both crystalline and aqueous phases.

2. Results and Discussion

2.1. Crystal Structures of PYR-MV Complexes

In **PYR$_a$-MV$_a$** with a chemical formula of $Na(C_{15}N_2H_{16})(C_{19}O_{10}S_3H_9)$, two sulfonate anions of PYR$_a^{3-}$ link with two crystallographic independent Na^+ ions to yield a 1D chain through strong O—Na bonds along the crystallographic *b*-axis, which was further connected into a 2D network via *bc* plane (**Figure 1a**; Table S1, Supporting Information).[34] We have calculated the distances and/or angles of $\pi...\pi$ interactions and

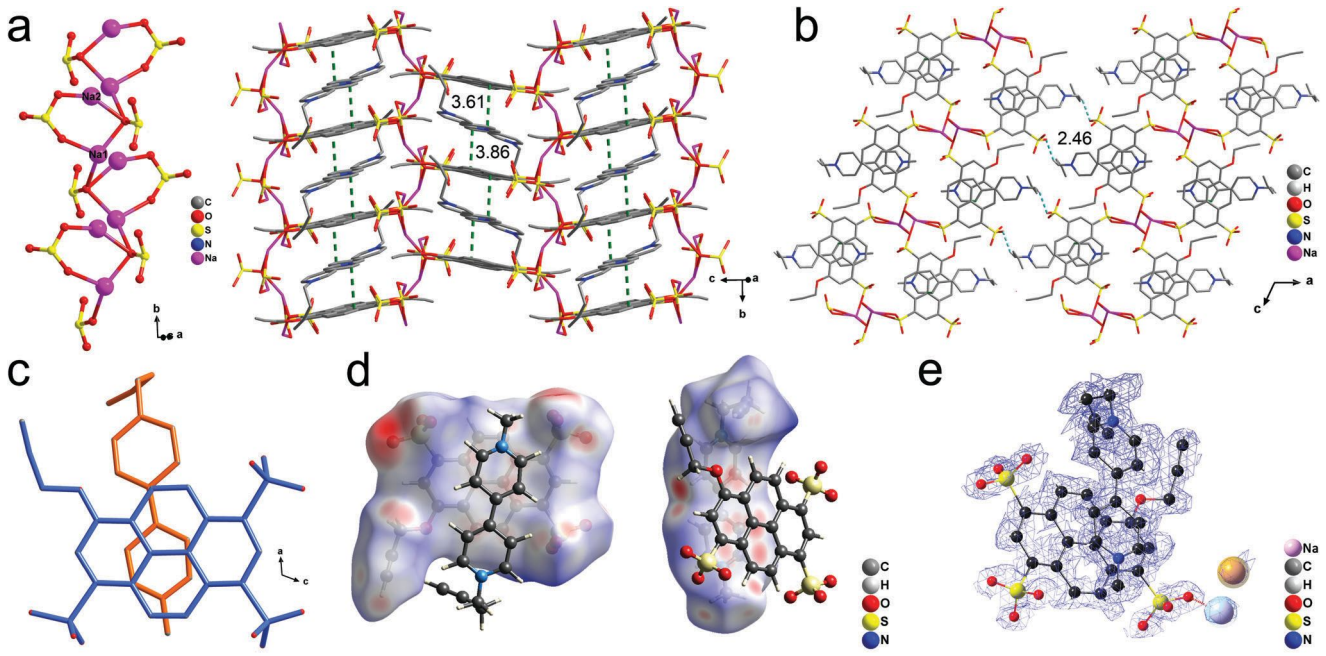

Figure 1. Crystal structure of $\mathbf{PYR_a\text{-}MV_a}$ complex. a) The coordination environments of Na1 and Na2, and the 2D network of $NaPYR_a^{2-}$ filled with MV_a^{2+} guest ions. b) The 3D framework of $\mathbf{PYR_a\text{-}MV_a}$ is stacked by the 2D networks via nonclassical hydrogen bonds. c) A projection of the 1:1 D–A pair from *b*-axis. The hydrogen atoms are omitted for clarity. d) Hirshfeld surface for the donor (left, $-0.85 < d_{norm} < 1.53$) and acceptor (right, $-0.45 < d_{norm} < 1.69$). Red, white, or blue surface color represents shorter, equal, or longer contact distance compared to the sum of the VDW radii, respectively. e) The electrostatic potential map from experimental data (isosurface value: 0.2 V).

hydrogen bonds through Platon (Tables S2 and S3, Supporting Information).[35] The MV_a^{2+} ions are intercalated into PYR_a^{3-} stacks and form a 1:1 mixed D–A–D–A 1D CT chain (π...π contacts, 3.61 and 3.86 Å). The adjacent 2D networks stack along *a*-axis, forming a 3D framework through nonclassical hydrogen bonds (H...O, 2.46 Å) (Figure 1b). Figure 1c shows the structure of one individual D–A pair, in which the π...π stacking deviates from the geometry center caused by the steric alkynyl group at the end of MV_a molecule. All of the hydrogen atoms were found during structural refinement. As shown in Figure 1d, the Hirshfeld surface (HS) was plotted for both donor and acceptor molecules over normalized contact distance, d_{norm}.[36,37] The darker red regions indicate the presence of the C—H...O hydrogen bonds and lighter ones are weaker short contacts. The π...π interaction between the donor and acceptor can be visualized by the triangular-shaped regions (highlighted by white dash circles) on the HS plotted over the shape index (Figure S1, Supporting Information). The π...π interaction areas deviated from the center of both donor and acceptor molecules, which is consistent with the off-center stacking geometry of D–A pair in Figure 1c. In the electrostatic potential map (Figure 1e), the electrostatic potential enveloped both the disordered Na^+ ions and all hydrogen atoms, which further proved the high accuracy of the refined structure.

Different from $\mathbf{PYR_a\text{-}MV_a}$, the unit cell of $\mathbf{PYR_b\text{-}MV_b}$ with a chemical formula of $(C_{12}N_2H_{14})_{1.5}(C_{16}O_{10}S_3H_7)$ contains one and a half MV_b^{2+} and one PYR_b^{3-}, and no host network is formed due to the lack of bridging Na^+ ions.[34] In **Figure 2**a, a similar 1:1 D–A–D–A 1D CT chain was formed between the neighboring PYR_b^{3-} and MV_b^{2+} (π...π contacts, 3.50 and 3.76 Å). The closer π...π packing in $\mathbf{PYR_b\text{-}MV_b}$ implies a stronger CT interaction than in $\mathbf{PYR_a\text{-}MV_a}$. We speculate that the closer packing in $\mathbf{PYR_b\text{-}MV_b}$ is the major reason for their structural difference, where there is not enough space to form a 1D sulfonate sodium chain. Instead of Na^+, an extra half MV_b^{2+} for charge balancing lies between the 1D chains without participating in the CT interaction. A similar structure was reported in the perylene-TCNQ crystals.[38] A 3D network is further formed via hydrogen bonds between sulfonate anion and hydroxy group (H...O, 2.11 Å) and nonclassical hydrogen bonds (H...O, 2.36 and 2.38 Å) between MV_b^{2+} and sulfonate anion (Figure 2b). From Figure 2c, we found the D–A pair in $\mathbf{PYR_b\text{-}MV_b}$ is more symmetrical and well aligned via the molecular center, compared to $\mathbf{PYR_a\text{-}MV_a}$. In Figure 2d, both C—H...O and O—H...O hydrogen bonds are presented as red areas in the HS plot. The shape index plot shows π...π interaction areas in $\mathbf{PYR_b\text{-}MV_b}$ are located more loosely (Figure S2, Supporting Information), compared with that in $\mathbf{PYR_a\text{-}MV_a}$ (Figure S1, Supporting Information). The interaction areas are also closer to the molecule centers, due to the higher symmetry. As shown in Figure 2e, H atoms are enveloped by the electrostatic potential, confirming the existence of H atoms from experimental data.

2.2. Electronic Structures of PYR-MV Complexes

From the crystal structure, we calculated the electronic structures of the two CTCs (**Figure 3**a,b). The two materials have similar electronic structures as indicated by the atom-projected density of states (PDOS). The states form a continuous band below −1 eV and have a series of intense peaks between −0.1 and 4 eV. The

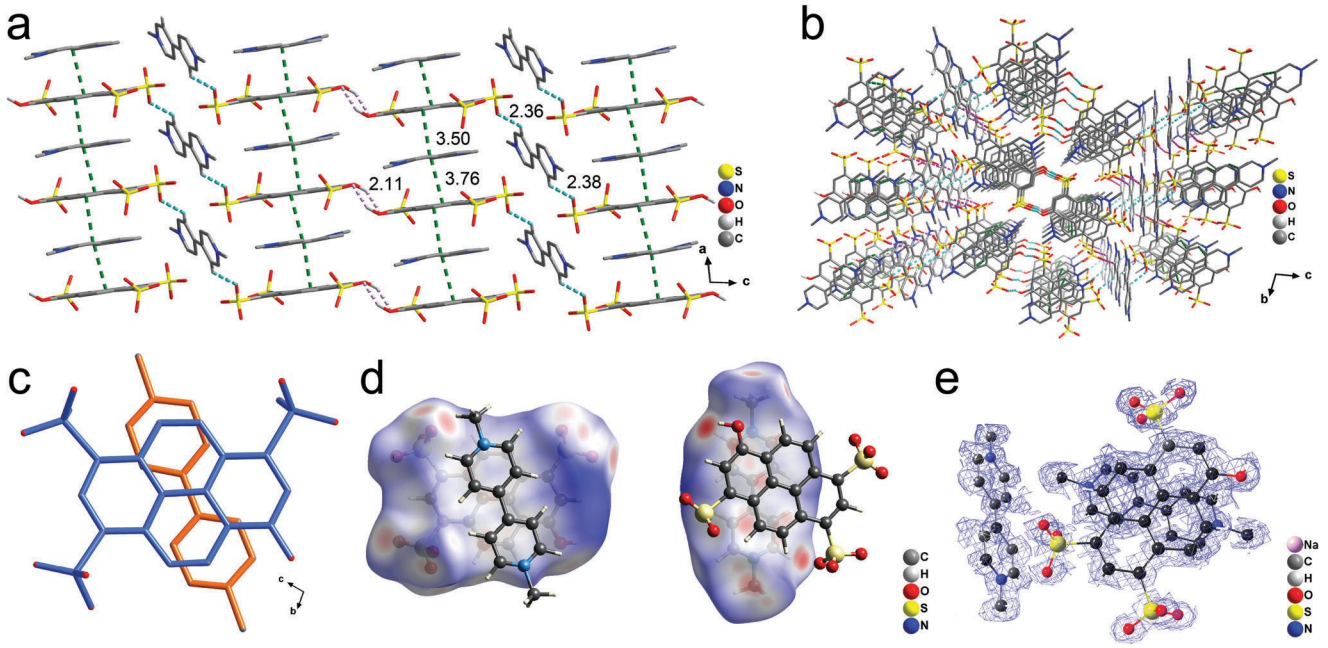

Figure 2. Crystal structure of $\mathbf{PYR_b\text{-}MV_b}$ complex. a) The 2D network is formed by 1D D–A–D–A 1D CT chains via classical and nonclassical hydrogen bonds. b) The 3D framework of $\mathbf{PYR_b\text{-}MV_b}$ is stacked by the 2D networks via nonclassical hydrogen bonds. c) A projection of the 1:1 D–A pair from *a*-axis. The hydrogen atoms are omitted for clarity. d) Hirshfeld surface for the donor molecule (left, $-1.21 < d_{norm} < 1.61$) and acceptor (right, $-0.806 < d_{norm} < 1.932$). Red, white, or blue surface color represents shorter, equal, or longer contact distance compared to the sum of the VDW radii, respectively. e) The electrostatic potential map from experimental data (isosurface value: 0.2 V).

states from C atoms are mixed throughout the energy range. The intense peak just below the Fermi level has contributions from O states and the sharp, unoccupied ones between 2.5 and 4 eV have contributions from H and N states. Thus, the charge is expected to transfer from the PYR electron donor to the MV electron acceptor. This is also illustrated by the charge density of the topmost occupied and bottom unoccupied bands in $\mathbf{PYR_a\text{-}MV_a}$ (Figure 3c,d). As expected, the charge density is located on the electron donor molecule in the topmost band and on the electron acceptor molecule in the bottom band. We also confirm that the extra half MV_b^{2+} in $\mathbf{PYR_b\text{-}MV_b}$ does not contribute to the CT interaction (Figure S3, Supporting Information).

The crystal conductivities along *a*, *b*, and *c* axes are obtained from the band structures (Figure S4, Supporting Information). Particularly, both crystals are more conductive along the D–A $\pi...\pi$ stacking direction, i.e., *b*-axis for $\mathbf{PYR_a\text{-}MV_a}$ and *a*-axis for $\mathbf{PYR_b\text{-}MV_b}$. The experimental conductivities (σ) of the two CTCs are measured from drop-casting thin films on a four-probe setup. The drop-cast thin films of the two complexes have the same structures as their crystals, which is confirmed by comparing the thin film X-ray diffraction patterns with the simulated XRD pattern from the crystallography structure (Figure S5, Supporting Information). The average isotropic conductivity of $\mathbf{PYR_a\text{-}MV_a}$ is $3.5 \pm 1.7 \times 10^{-4}$ S m^{-1} from six individual samples with a thickness of 300–500 nm (Figure S6, Supporting Information). The conductivity of $\mathbf{PYR_b\text{-}MV_b}$ is much lower ($\sigma < 4 \times 10^{-7}$ S m^{-1}). The conductivity difference in the two complexes indicates the structure of the crystal and the donor can largely tune the conductivity of CTCs.[39,40] We then compare the experimental conductivity with the calculated isotropic conductivity (Figure 3e,f), which is the mean conductivity in different directions. Assuming both CTCs are *p*-type doping as typical in organic crystals,[41] we speculate the band transport is the major transport mechanism and the conduction is occurring at $E - E_F < -0.6$ eV, where the calculated conductivities of $\mathbf{PYR_a\text{-}MV_a}$ is higher than that of $\mathbf{PYR_b\text{-}MV_b}$, consistent with the measured values. Both crystals are indirect gap materials as seen in the electronic band structure (Figure S7, Supporting Information). The band dispersion near the Fermi level is weak and likely limits the electrical conductivity via band transport. However, there are direct transitions at slightly higher energy. The lowest energy transition is 2.59 eV from Γ to D in $\mathbf{PYR_a\text{-}MV_a}$ and 2.58 eV from Y to U in $\mathbf{PYR_b\text{-}MV_b}$. The direct bandgap is at the Γ-point and is 2.62 eV and 2.73 eV for $\mathbf{PYR_a\text{-}MV_a}$ and $\mathbf{PYR_b\text{-}MV_b}$, respectively.

2.3. UV–Vis and PL Study of PYR-MV Complexes

Spectroscopy characterizations, i.e., UV–vis and PL are employed to further investigate the CT interactions in both solid-state and aqueous phases. We have acquired the solid-state UV–vis and PL spectra from thin film samples drop-cast from the solutions of PYRs, MVs, or their 1:1 mixture. From UV–vis spectra (**Figure** 4a,b), we can clearly observe a CT band at ca. 460–480 nm in both $\mathbf{PYR_a\text{-}MV_a}$ and $\mathbf{PYR_b\text{-}MV_b}$. The CT peak is more intensive in $\mathbf{PYR_b\text{-}MV_b}$ than in $\mathbf{PYR_a\text{-}MV_a}$, in consistency with the stronger CT interaction between PYR_b^{3-} and MV_b^{2+} from structural analysis. The quenching effect of PYR by MV was observed in the solid-state PL of both $\mathbf{PYR_a\text{-}MV_a}$ and $\mathbf{PYR_b\text{-}MV_b}$, indicating the CT interaction between PYRs and MVs (Figure 4c,d).

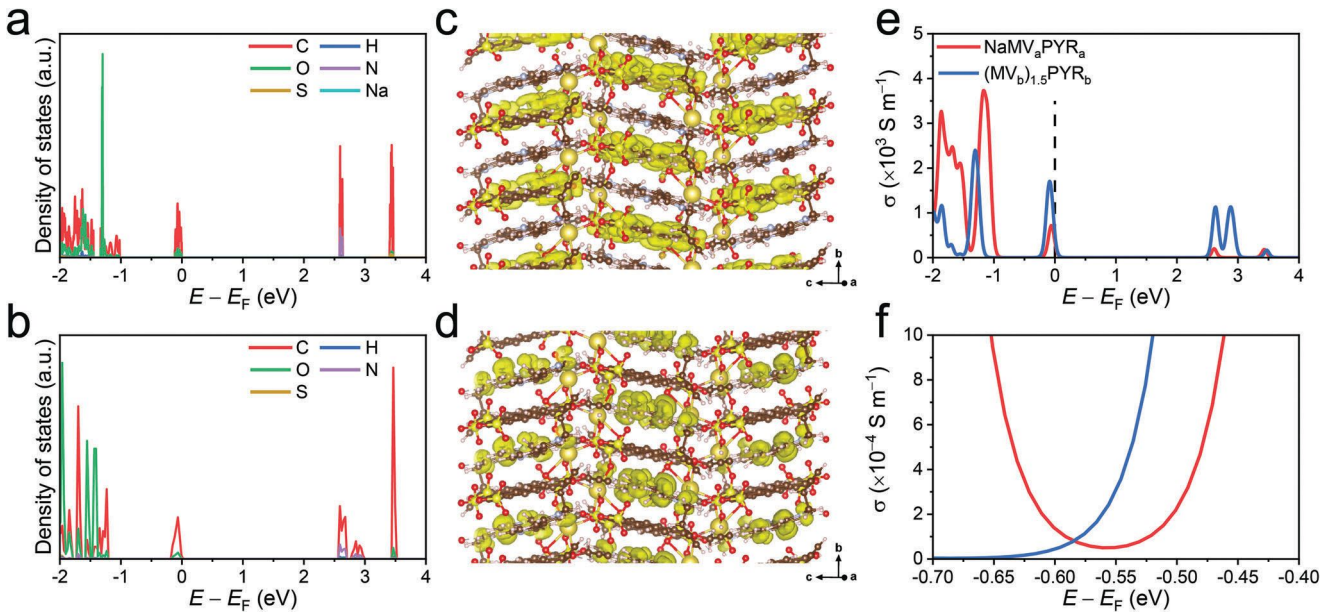

Figure 3. The calculated atom projected density of states (PDOS) of crystals a) **PYR_a-MV_a** and b) **PYR_b-MV_b**. The band-projected charge density of the c) topmost occupied band and d) bottom unoccupied band of **PYR_a-MV_a**. The isovalue is 1×10^{-3} $e\ a_0^{-3}$. e) Calculated isotropic electric conductivity of **PYR_a-MV_a** and **PYR_b-MV_b**. f) The zoom in conductivity between −0.7 and −0.4 eV.

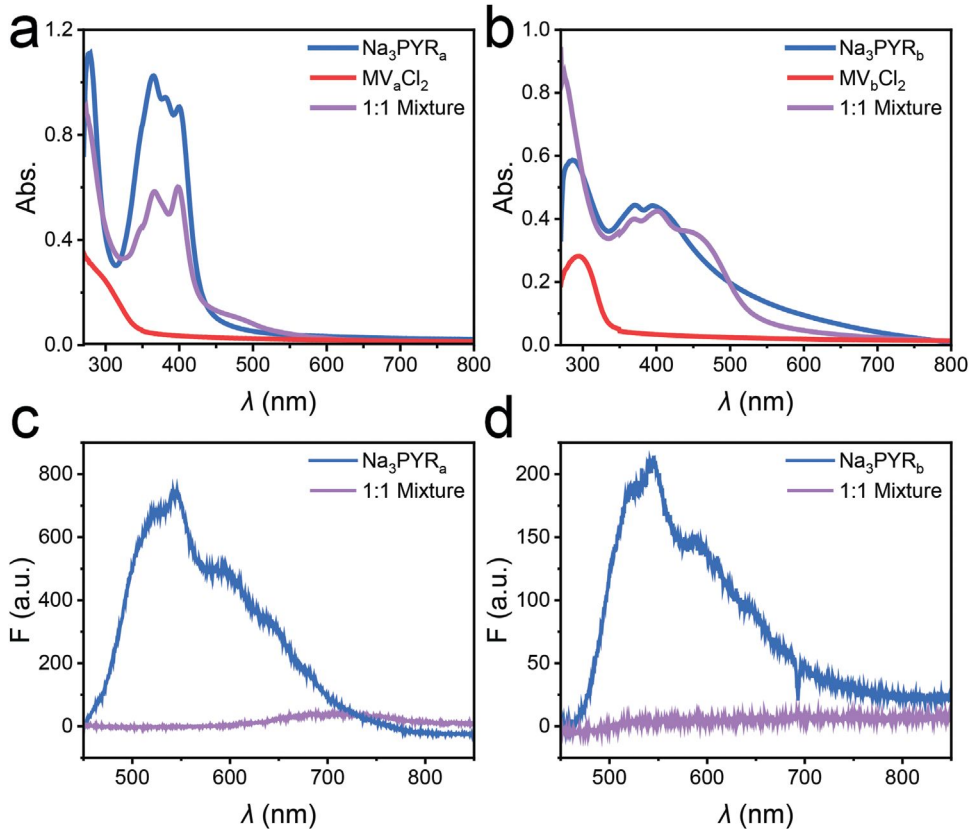

Figure 4. Solid-state UV–vis spectra of a) Na_3PYR_a, MV_aCl_2, and their 1:1 mixture. b) Na_3PYR_b, MV_bCl_2, and their 1:1 mixture. Photoluminescence spectra of c) Na_3PYR_a and its 1:1 mixture with MV_aCl_2. d) Na_3PYR_b and its 1:1 mixture with MV_bCl_2. The samples are prepared by drop casting 50 µL of 0.01 M solution on a 1.5 cm × 1.5 cm cover glass pretreated with O_2 plasma.

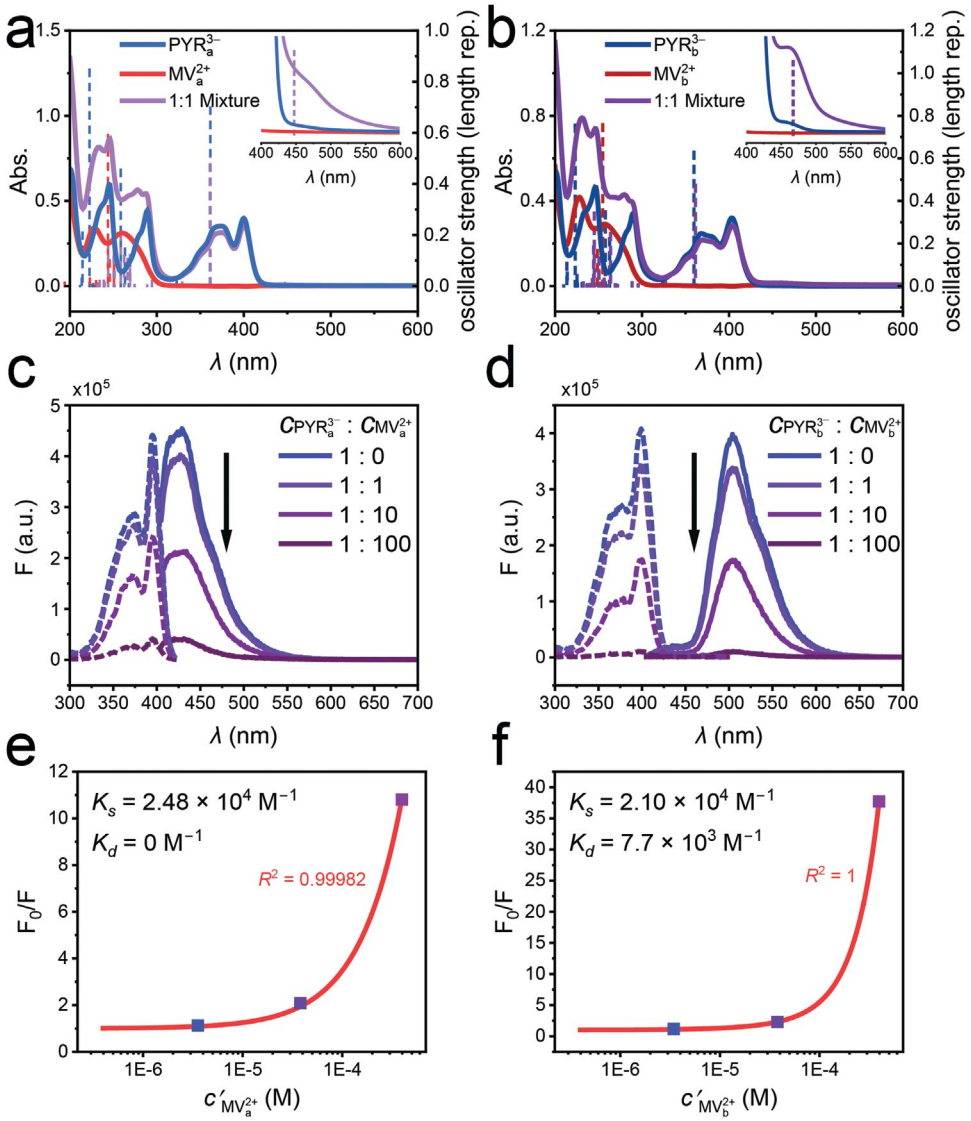

Figure 5. UV–vis spectra of a) PYR$_a^{3-}$-MV$_a^{2+}$, and b) PYR$_b^{3-}$-MV$_b^{2+}$ in water. The concentrations were 2×10^{-5} M (main) and 1.67×10^{-3} M (inset). The TD-DFT calculated electronic excitations were plotted as vertical dash lines with the same color. PL spectra of c) PYR$_a^{3-}$-MV$_a^{2+}$, and d) PYR$_b^{3-}$-MV$_b^{2+}$ with different concentration ratios in water. The initial concentration for PYRs (c_0) is 4×10^{-6} M. The emission spectra (solid curve) were excited by 395 nm light, and the excitation spectra used a maximum emission of 430 nm for PYR$_a^{3-}$-MV$_a^{2+}$ and 510 nm for PYR$_b^{3-}$-MV$_b^{2+}$. e,f) are the plots and fitting curves of the ratio of initial PL intensity (F_0) to quenched PL intensity (F) as a function of the concentration of unassociated MVs ($c'_{MV_a^{2+}}$ or $c'_{MV_b^{2+}}$, plotted in logarithmic scale).

A more efficient quenching was found in **PYR$_b$-MV$_b$** than in **PYR$_a$-MV$_a$**, evidenced by the incomplete quenched peak at ca. 700 nm in the 1:1 mixture of PYR$_a^{3-}$ and MV$_a^{2+}$ (Figure S8, Supporting Information). This is also caused by the closer packing and stronger CT interaction of PYR$_b^{3-}$ and MV$_b^{2+}$ in the crystal structure.

The CT interaction between PYRs and MVs in the aqueous phase is crucial for their functional and structural diversity,[17,42] thus important to investigate. Besides, the samples are dispersed homogenously in the liquid state, providing more reliable data for quantitative analysis. From UV–vis spectra of the 1:1 mixture of PYRs and MVs at high concentration, a clear characteristic band at ca. 470 nm representing the intermolecular CT was observed as the purple curve shown in **Figure 5**.[43] We also found that the PYR$_b^{3-}$ itself has a weak intermolecular CT indicated by the weak CT bands at 460 nm as the blue curve shown in the insets of Figure 5b. However, this CT band was inhibited in PYR$_a^{3-}$ due to the existence of the propargyl group. The CT bands in **PYR$_b$-MV$_a$/MV$_b$** complexes are stronger than those in **PYR$_a$-MV$_a$/MV$_b$** complexes (Figure 5; Figure S9, Supporting Information), also indicating a decreased donor ability of PYR$_a^{3-}$ due to the steric effect of the propargyl group. The UV–vis spectra of PYR$_a^{3-}$ and PYR$_b^{3-}$ are very similar, implying a similar molecular orbital structure.

The electronic excitations of the CTCs were further examined using TD-DFT with a range-separated hybrid functional,

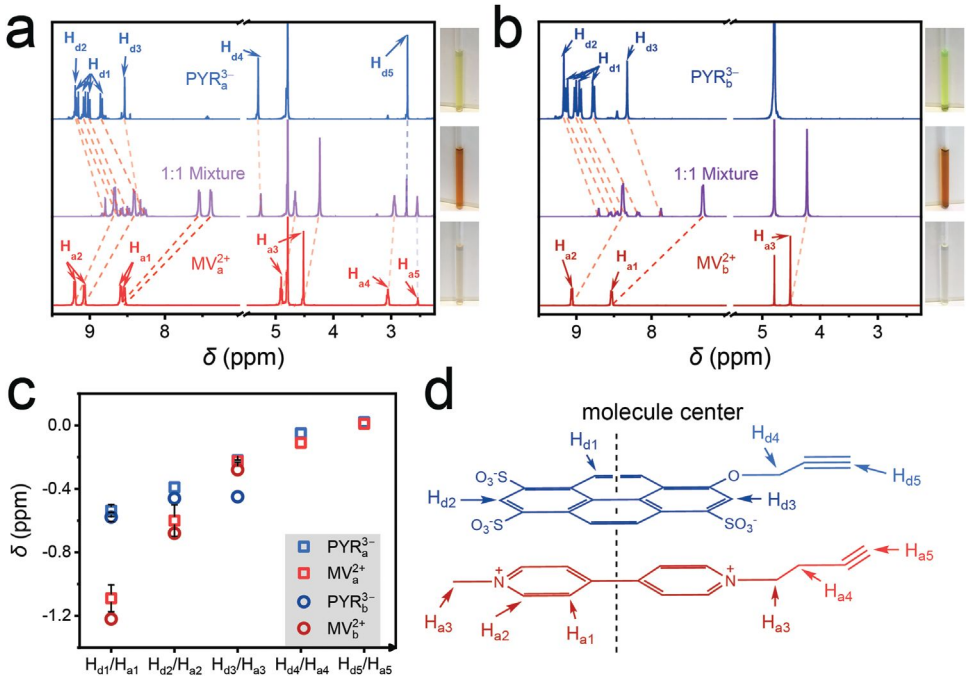

Figure 6. NMR and photos of a) PYR_a^{3-}-MV_a^{2+}, and b) PYR_b^{3-}-MV_b^{2+} donor-acceptor pairs in D_2O, with all concentrations of 0.01 M (solvent peak of H_2O, 4.8 ppm). The ^1H atoms were numbered and marked as H_{an} or H_{dn} in the chemical structures in (d). The red and blue dash lines indicate chemical shifts of ^1H atoms to the upfield and downfield, respectively. c) Chemical shift value of ^1H atoms in **PYR_a-MV_a** (hollow squares) and **PYR_b-MV_b** (hollow circles) complexes. The error bars represent the standard deviations of multiple ^1H atoms. d) Schematic illustration of a PYR_a^{3-} (dark blue and blue)/PYR_b^{3-} (dark blue) and MV_a^{2+} (dark red and red)/MV_b^{2+} (red) complex.

which has been shown to reliably and accurately predict electronic spectra.[29–32] The calculations show that the band on the low-energy shoulder is a CT excitation. The **PYR_a-MV_a** complex had electronic transition energies of 447 and 361 nm from the ground state to the S_1 and S_2 excited states, respectively. The electron density difference of the $S_0 \rightarrow S_1$ excitation reveals that electronic charge is shifted from the PYR electron donor to the MV electron acceptor (Figure S10, Supporting Information). The oscillator strength of the CT excitation was weaker than the intramolecular $S_0 \rightarrow S_2$ electronic excitation (vertical dash lines in Figure 5a). These findings are consistent with the appearance of the low-energy band in the experimental spectra. Similar results were obtained for the **PYR_b-MV_b** complex. The lowest-energy electronic excitations occur at 467 and 361 nm and CT occurs in the $S_0 \rightarrow S_1$ excitation. The binding energies of the complexes show that their formation is energetically favorable (−59 and −67 kJ mol^{-1} for the **PYR_a-MV_a** and **PYR_b-MV_b** complexes, respectively). A stronger bonding energy in **PYR_b-MV_b** is consistent with its stronger CT band compared to **PYR_a-MV_a**.

Figure 5c,d show the PL spectra of PYRs with different amounts of added MVs, as the ratio of initial PL intensity (F_0) to quenched PL intensity (F) of PYRs can indicate the ratio of PYR-MV complexes concentration ($c_{complex}$) to the initial PYRs concentration ($c_{PYR}{}^{3-}$) where $c_{PYR}{}^{3-}/c_{complex} = 1–F_0/F$.[44] Then we can get the concentration of unassociated MVs ($c'_{MV}{}^{2+}$) as $c'_{MV}{}^{2+} = c_{MV}{}^{2+} - c_{complex}$, where $c_{MV}{}^{2+}$ is the initial MVs concentration. The ratio of F_0 to F as a function of the concentration of unassociated MVs ($c'_{MVa}{}^{2+}$ or $c'_{MVb}{}^{2+}$) was plotted in Figure 5e,f. By fitting the data with a parabola function:

$$\frac{F_0}{F} = 1 + (K_s + K_d)\, c'_{MV} + K_s K_d c'_{MV}{}^2 \quad (1)$$

where K_s and K_d are the static and dynamic quenching constant respectively.[42] In the case of PYR_a^{3-}-MV_a^{2+}, we observe a linear relationship between F_0/F and $c'_{MVa}{}^{2+}$ where the slope K_s is 2.48×10^4 M^{-1} and K_d is 0 M^{-1}, indicating an absence of the dynamic quenching process.[44] In the case of PYR_b^{3-}-MV_b^{2+}, we got a K_s of 2.10×10^4 M^{-1} and a K_d of 7.7×10^3 M^{-1}, consistent with previous findings.[42] We speculate that the extra half acceptor in the crystal structure of **PYR_b-MV_b** contributes to this dynamic quenching process. The maximum emission also blue-shifted dramatically from 430 nm in PYR_a^{3-} to 510 nm PYR_b^{3-} which consists of the previously reported amphiphilic pyranines.[45]

2.4. NMR Study of PYR-MV Complexes

For further studying the structures of CTCs in the aqueous phase, we performed the ^1H NMR for PYRs, MVs, and their 1:1 mixture in D_2O and analyzed the chemical shifts (**Figure 6**). In Figure 6a,b, we have observed an obvious upfield chemical shifting of ^1H on pyrene of PYRs and pyridine of MVs, meaning the shielding effect is mainly from the $\pi...\pi$ stacking of the donor

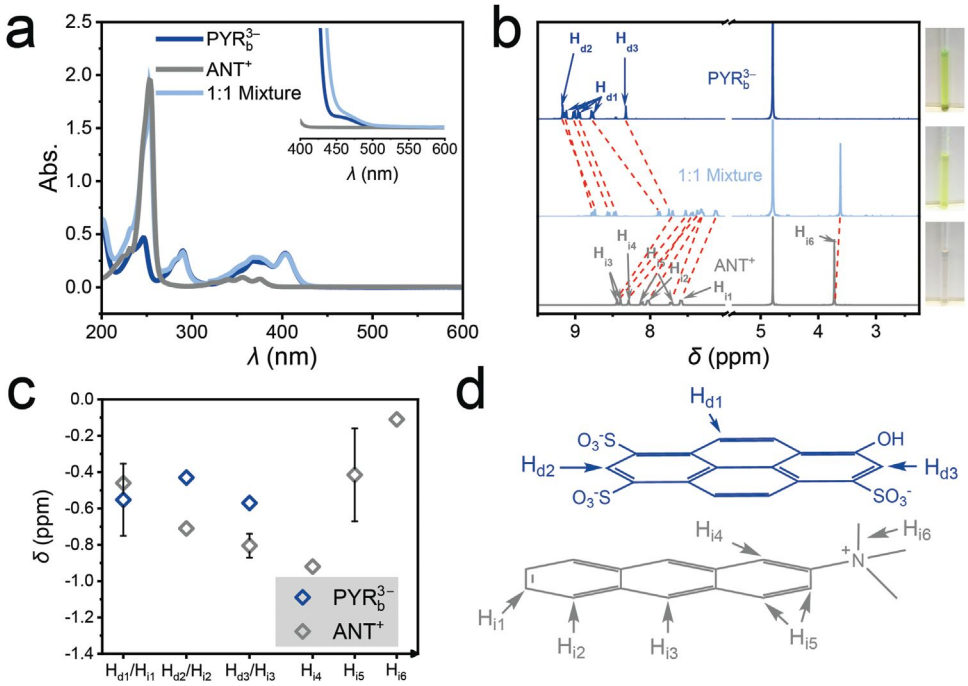

Figure 7. a) UV–vis spectra of PYR_b^{3-} and ANT^+ in water. The concentrations were 2×10^{-5} M (main) and 1.67×10^{-3} M (inset). b) NMR and photos of PYR_b^{3-} and ANT^+ in D_2O, with all concentrations of 0.01 M (solvent peak of H_2O, 4.8 ppm). The ^1H atoms on the PYR or ANT molecules were numbered and marked as H_{an} or H_{in} respectively, in the chemical structures in (**d**). The red dash lines indicate chemical shifts of ^1H atoms to the upfield. c) Chemical shift value of ^1H atoms in PYR_b^{3-} and ANT^+. The error bars represent the standard deviations of multiple ^1H atoms. d) Schematic illustration of a PYR_b^{3-} (dark blue) and ANT^+ (grey).

and acceptor conjugated systems. The high-concentration mixtures of PYRs and MVs have a brown color, which changed dramatically from the original color of PYRs and MVs, indicating strong intermolecular CT interactions between the donors and acceptors.

We can also obtain geometric information on the CTCs from the chemical shifting patterns by plotting the chemical shift of ^1H located on different parts of the molecules (Figure 6c). In both **PYR_a-MV_a** and **PYR_b-MV_b** complexes, H_{d1} and H_{a1} atoms which are closest to the molecule center of the PYRs and MVs have a larger chemical shift to the upfield due to a stronger shielding effect (−0.54 to −0.58 ppm for H_{d1}, −1.09 to −1.22 ppm for H_{a1}). There is a very clear trend that the chemical shift values decrease with the increasing distance of ^1H atoms from the molecule center. In the end, the hydrogens on terminal alkynes (H_{d5} and H_{a5}) have an un-shielding effect where the chemical shifts moved slightly to the downfield direction (0.02 for H_{d5}, 0.01 for H_{a5}). In general, it is most likely that the CTCs of PYRs and MVs molecules were formed via $\pi...\pi$ stacking of their conjugated systems with an overlapping molecule center as indicated in Figure 6d. The chemical shifts of H_{d2} and H_{d3} which have similar distances to the molecule center were different in PYR_a^{3-}-MV_a^{2+} but similar in PYR_b^{3-}-MV_b^{2+}, meaning the PYR_b^{3-}-MV_b^{2+} complex is more aligned to the molecule center due to its higher symmetry. This observation consists very well with their crystal structures (Figures 1c and 2c). On the other hand, all the chemical shift values in **PYR_b-MV_b** complex (hollow circles) are larger than in **PYR_a-MV_a** complex (hollow squares), indicating a stronger interaction, which is consistent with the results from UV–vis, PL measurements, and DFT calculation. In Figure S11 (Supporting Information), we also studied the chemical shift of **PYR_a-MV_b** and **PYR_b-MV_a** complexes. The same trend was observed where the center H atoms have a higher chemical shift.

The derivatives of anthracene are common electron donors in CT pairs. However, in the UV–vis and ^1H NMR of the mixture of ANT^+ and MVs (Figure S12, Supporting Information), no CT band or ^1H chemical shift was observed, meaning ANT^+ (Scheme 1a) lost the electron donor property when introducing a quaternary amino group on the α position. We have also studied the interaction between PYR_b^{3-} and ANT^+ as shown in the UV–vis and ^1H NMR data in **Figure 7**. In the UV–vis spectra (Figure 7a), there was no obvious CT band in the 1:1 mixture of PYR_b^{3-} and ANT^+ indicating the absence of CT interaction. Although without any color change, we have observed a notable ^1H chemical shift when mixing PYR_b^{3-} and ANT^+ (Figure 7b), caused by the shielding effect from the electrostatic attraction of the oppositely charged molecules. By studying the chemical shift pattern (Figure 7c), we found regions close to H_{d1} and H_{d3} in PYR_b^{3-} and H_{n4} in ANT^+ encountered the largest shielding effect as the green shaded area marked in Figure 7d. These areas are likely to overlap due to electrostatic attraction. Our attempt to crystalize PYR_b^{3-} and ANT^+ has failed. These results implied that the opposite charge or the existence of electron donor/acceptor moiety does not necessarily lead to CT interaction between two conjugated systems, implying rational molecular design is important for water-based CTCs.

Table 1. A comparison of major characteristics of PYR_a-MV_a and PYR_b-MV_b complexes.

Characteristics	PYR_a-MV_a	PYR_b-MV_b
Chemical formula	$Na(C_{15}N_2H_{16})(C_{19}O_{10}S_3H_9)$	$(C_{12}N_2H_{14})_{1.5}(C_{16}O_{10}S_3H_7)$
Structural topology	2D host-guest network	1D chain
$\pi...\pi$ contact distance	3.61 and 3.86 Å	3.50 and 3.76 Å
CT mechanism	PYR_a to MV_a	PYR_b to MV_b
CT excitation	$S_0 \rightarrow S_1$	$S_0 \rightarrow S_1$
Calculated direct bandgap	2.62 eV	2.73 eV
Calculated binding energy	−59 kJ mol^{-1}	−67 kJ mol^{-1}
Conductivity mechanism	Band transport below E_F	Band transport below E_F
Experimental conductivity	$3.5 \pm 1.7 \times 10^{-4}$ S m^{-1}	$<4 \times 10^{-7}$ S m^{-1}
CT interaction in solid-state	Weaker	Stronger
CT interaction in the aqueous phase	Weaker	Stronger
D–A pair geometry in solid state	Nonsymmetric	Symmetric
D–A pair geometry in the aqueous phase	Nonsymmetric	Symmetric
PL quenching in the aqueous phase	Static quenching	Static and dynamic quenching

3. Conclusion

We have determined the crystal structures and obtained the entire range of noncovalent interactions of two submicron-sized crystals (**PYR_a-MV_a** and **PYR_b-MV_b**) using 3DED. Our efforts of combining experiments and DFT calculation also enable us to quantitatively analyze the physical properties in both solid state and aqueous phase. Owing to the various molecular designs, distinct structural topologies and/or symmetries were found in their crystal structures and complexes in the aqueous phase. The different CT intensities in the two complexes lead to various physical properties, e.g., conductivities, CT absorption intensity, PL quenching, etc., which were confirmed experimentally and theoretically in both phases. To be more specific, we have listed the detailed characteristics of the two CT complexes in **Table 1**. Besides, the spectroscopy study of PYR_b^{3-} and ANT^+ also suggests that electrostatic interaction between conjugated molecules does not adequately allow intermolecular CT.

In summary, we have demonstrated how the structure and properties of crystalline CT materials, especially for small crystals that cannot be investigated by X-ray diffraction, can be investigated by a combination of 3DED, spectroscopy, and DFT calculation. The novel insights into the structure and properties of crystalline CT materials could advance the use of crystal engineering for various applications, i.e., organic electronics.

Supporting Information

Supporting Information is available from the Wiley Online Library or from the author.

Acknowledgements

This work was supported by the Academy of Finland (Z.-P.L. No. 330214; T.-P. R. No. 340103; Center of Excellence Program in Life-inspired Hybrid Materials, LIBER No. 346107 and 346108; Flagship Competence Center for Materials Bioeconomy, FinnCERES No. 318890 and 318891), EU H2020 Marie Skłodowska-Curie grant (T.-P. R. No. 101022777; T.Y. No. 101146059), National Natural Science Foundation of China (H.-Y.W. No. 21801127), The Swedish Research Council (H.X. No. 2017–05333; L.B. No. 2019-05624), The Swedish Research Council for Environment, Agricultural Sciences and Spatial Planning (T.Y. No. 2022–02778), The Royal Swedish Academy (T.Y. No. CH2022-0015 and PH2022-0021), The Science for Life Laboratory through the technique development grant (MicroED@SciLifeLab). The authors thank Dr. X. Bai for his assistance in the electric property test of the crystals. The authors acknowledge the Finnish IT Center for Science (CSC) for computational resources.

Conflict of Interest

The authors declare no conflict of interest.

Data Availability Statement

The data that support the findings of this study are available from the corresponding author upon reasonable request.

Keywords

3D electron diffraction, charge-transfer, crystal, density functional theory, noncovalent interaction

Received: September 12, 2023
Revised: March 3, 2024
Published online: March 25, 2024

[1] M. J. S. Dewar, *Molecular Orbital Theory of Organic Chemistry*, McGraw Hill, New York **1969**.
[2] U. M. Rabie, *J. Mol. Struct.* **2013**, *1034*, 393.
[3] D. Shen, W.-C. Chen, M.-F. Lo, C.-S. Lee, *Mater. Today Energy* **2021**, *20*, 100644.
[4] Y. Takahashi, T. Hasegawa, Y. Abe, Y. Tokura, K. Nishimura, G. Saito, *Appl. Phys. Lett.* **2005**, *86*, 063504.
[5] A. S. Tayi, A. K. Shveyd, A. C.-H. Sue, J. M. Szarko, B. S. Rolczynski, D. Cao, T. J. Kennedy, A. A. Sarjeant, C. L. Stern, W. F. Paxton, W. Wu, S. K. Dey, A. C. Fahrenbach, J. R. Guest, H. Mohseni, L. X. Chen, K. L. Wang, J. F. Stoddart, S. I. Stupp, *Nature* **2012**, *488*, 485.

[6] L. Zhan, S. Li, Y. Li, R. Sun, J. Min, Y. Chen, J. Fang, C. Ma, G. Zhou, H. Zhu, L. Zuo, H. Qiu, S. Yin, H. Chen, *Adv. Energy Mater.* **2022**, *12*, 2201076.
[7] K. Goushi, K. Yoshida, K. Sato, C. Adachi, *Nat. Photonics* **2012**, *6*, 253.
[8] X.-K. Liu, Z. Chen, C.-J. Zheng, M. Chen, W. Liu, X.-H. Zhang, C.-S. Lee, *Adv. Mater.* **2015**, *27*, 2025.
[9] Q. Xue, G. Xie, *Adv. Opt. Mater.* **2021**, *9*, 2002204.
[10] J. Zhang, W. Xu, P. Sheng, G. Zhao, D. Zhu, *Acc. Chem. Res.* **2017**, *50*, 1654.
[11] K. P. Goetz, H. F. Iqbal, E. G. Bittle, C. A. Hacker, S. Pookpanratana, O. D. Jurchescu, *Mater. Horiz.* **2022**, *9*, 271.
[12] L. Sun, Y. Wang, F. Yang, X. Zhang, W. Hu, *Adv. Mater.* **2019**, *31*, 1902328.
[13] M. E. Gershenson, V. Podzorov, A. F. Morpurgo, *Rev. Mod. Phys.* **2006**, *78*, 973.
[14] W. Zhu, R. Zheng, X. Fu, H. Fu, Q. Shi, Y. Zhen, H. Dong, W. Hu, *Angew. Chemie* **2015**, *127*, 6889.
[15] H. T. Black, D. F. Perepichka, *Angew. Chem., Int. Ed.* **2014**, *53*, 2138.
[16] Y. Kang, X. Tang, Z. Cai, X. Zhang, *Adv. Funct. Mater.* **2016**, *26*, 8920.
[17] M. Kumar, K. Venkata Rao, S. J. George, *Phys. Chem. Chem. Phys.* **2014**, *16*, 1300.
[18] Z. P. Lv, B. Chen, H. Y. Wang, Y. Wu, J. L. Zuo, *Small* **2015**, *11*, 3597.
[19] S. Gamsey, A. Miller, M. M. Olmstead, C. M. Beavers, L. C. Hirayama, S. Pradhan, R. A. Wessling, B. Singaram, *J. Am. Chem. Soc.* **2007**, *129*, 1278.
[20] M. Ge, T. Yang, H. Xu, X. Zou, Z. Huang, *J. Am. Chem. Soc.* **2022**, *144*, 15165.
[21] S. Seo, T. Yang, J. Shin, D. Jo, X. Zou, S. B. Hong, *Angew. Chem.* **2018**, *130*, 3789.
[22] B. Wang, T. Rhauderwiek, A. K. Inge, H. Xu, T. Yang, Z. Huang, N. Stock, X. Zou, *Chem. – A Eur. J.* **2018**, *24*, 17429.
[23] T. Yang, T. Willhammar, H. Xu, X. Zou, Z. Huang, *Nat. Protoc.* **2022**, *17*, 2389.
[24] T. Yang, S. Waitschat, A. K. Inge, N. Stock, X. Zou, H. Xu, *Symmetry* **2021**, *13*, 2131.
[25] H. Xu, H. Lebrette, T. Yang, V. Srinivas, S. Hovmöller, M. Högbom, X. Zou, *Structure* **2018**, *26*, 667.
[26] L. Palatinus, P. Brázda, P. Boullay, O. Perez, M. Klementová, S. Petit, V. Eigner, M. Zaarour, S. Mintova, *Science* **2017**, *355*, 166.
[27] K. Yonekura, K. Kato, M. Ogasawara, M. Tomita, C. Toyoshima, *Proc. Natl. Acad. Sci.* **2015**, *112*, 3368.
[28] P. Brázda, L. Palatinus, M. Babor, *Science* **2019**, *364*, 667.
[29] M. Fumanal, C. Corminboeuf, B. Smit, I. Tavernelli, *Phys. Chem. Chem. Phys.* **2020**, *22*, 19512.
[30] F. Lipparini, B. Mennucci, *J. Chem. Phys.* **2016**, *144*, 160901.
[31] N. T. Maitra, *J. Phys. Condens. Matter.* **2017**, *29*, 423001.
[32] T. Stein, L. Kronik, R. Baer, *J. Am. Chem. Soc.* **2009**, *131*, 2818.
[33] A. K. Jeevan, K. R. Gopidas, *J. Phys. Chem. B* **2021**, *125*, 4428.
[34] The Cambridge Crystallographic Data Center (CCDC) Deposition Numbers of PYRa-MVa and PYRb-MVb Complexes Are CCDC 2126009 and 2126010, Respectively., n.d.
[35] A. L. Spek, *Acta Crystallogr. Sect. D Biol. Crystallogr.* **2009**, *65*, 148.
[36] M. A. Spackman, D. Jayatilaka, *CrystEngComm* **2009**, *11*, 19.
[37] P. R. Spackman, M. J. Turner, J. J. McKinnon, S. K. Wolff, D. J. Grimwood, D. Jayatilaka, M. A. Spackman, *J. Appl. Crystallogr.* **2021**, *54*, 1006.
[38] A. W. Hanson, *Acta Crystallogr. Sect. B Struct. Crystallogr. Cryst. Chem.* **1978**, *34*, 2339.
[39] K. P. Goetz, D. Vermeulen, M. E. Payne, C. Kloc, L. E. McNeil, O. D. Jurchescu, *J. Mater. Chem. C* **2014**, *2*, 3065.
[40] H. Kisch, B. Eisen, R. Dinnebier, K. Shankland, W. I. F. F. David, F. Knoch, *Chem. – A Eur. J.* **2001**, *7*, 738.
[41] H. Klauk, *Chem. Soc. Rev.* **2010**, *39*, 2643.
[42] E. B. de Borba, C. L. C. Amaral, M. J. Politi, R. Villalobos, M. S. Baptista, *Langmuir* **2000**, *16*, 5900.
[43] C. Wang, Y. Guo, Y. Wang, H. Xu, R. Wang, X. Zhang, *Angew. Chem., Int. Ed.* **2009**, *48*, 8962.
[44] D. B. Cordes, S. Gamsey, Z. Sharrett, A. Miller, P. Thoniyot, R. A. Wessling, B. Singaram, *Langmuir* **2005**, *21*, 6540.
[45] R. Sasaki, S. Murata, *Langmuir* **2008**, *24*, 2387.

